

Entanglement structure of the Hubbard model in momentum space

G. Ehlers¹, J. Sólyom², Ö. Legeza², R. M. Noack¹

¹ *Fachbereich Physik, Philipps-Universität Marburg, 35032 Marburg, Germany*

² *Strongly Correlated Systems “Lendület” Research group,
Wigner Research Centre for Physics, H-1525 Budapest, Hungary*

(Dated: October 1, 2018)

We study the properties of the ground states of the one- and two-dimensional Hubbard models at half-filling and moderate doping using entanglement-based measures, which we calculate numerically using the momentum-space density matrix renormalization group (DMRG). In particular, we investigate quantities such as the single-site entropy and two-site mutual information of single-particle momentum states as well as the behavior of the bipartite subsystem entropy for partitions in momentum space. The distribution of these quantities in momentum space gives insight into the fundamental nature of the ground state, insight that can be used to make contact with weak-coupling-based analytic approaches and to optimize numerical methods, the momentum-space DMRG in particular. We study the site and subsystem entropies as a function of interaction strength U and system size. In both the one- and two-dimensional cases, we find that the subsystem entropy scales proportionally to U^2 for weak U and proportionally to volume. Nevertheless, the optimized momentum-space DMRG can provide variationally accurate results for the two-dimensional Hubbard model at weak coupling for moderate system sizes.

PACS numbers: 71.10.Fd, 71.27.+a

I. INTRODUCTION

Simulating quantum systems on classical computers is a major challenge in theoretical physics, a challenge that has been addressed by a number of recent algorithmic developments [1, 2]. Such simulation is particularly difficult when strong correlations, as reflected in a high level of entanglement, are present [3]. For one-dimensional systems, the matrix-product-state-based (MPS-based) [4, 5] density matrix renormalization group (DMRG) method [6] is the most effective tool to calculate the properties of the ground and selected excited states. In higher dimensions, the DMRG is less efficient at representing the entanglement structure of states due to its one-dimensional topology. Recent developments have led to several alternative methods that potentially overcome the limitations of the DMRG. These include, tensor network states (TNS) [7], the multi-scale entanglement renormalization (MERA) [8], the projected entangled pair states (PEPS) [9], the tree-tensor network state (TTNS) [10], quantum Monte Carlo (QMC) [11–15], and the density matrix embedding theory (DMET) [16, 17]. All such methods have advantages and disadvantages; each of these methods has competitive performance in particular circumstances. However, there is no single method yet that can be applied efficiently as a black-box tool to a general quantum lattice problem. Therefore, despite substantial effort over many years, accessible system sizes in more than one dimension are still strongly limited.

For example, in two and higher dimensions, QMC is a potentially very powerful method but it suffers from the so-called fermion sign problem [13, 18, 19], which occurs when fermionic systems and spin systems with frustration are treated. The domain of application of PEPS is

limited due to the expensive scaling of the computational cost with bond dimension when highly entangled systems are treated [9, 20]. In addition, when the infinite-system version of PEPS, iPEPS, is used, the proper choice of the size of the unit cell can significantly effect the final solution [21]. Another promising method for simulating two-dimensional systems is the DMET, a method that is based on the numerically exact calculation of the ground state (or other particular state) of a finite-size cluster embedded to an environment via a density matrix. The cluster calculation is typically carried out using exact diagonalization or the DMRG, whereas the degrees of freedom of the environment are approximated. The accuracy therefore depends on the level of truncation of the environment degrees of freedom. Within the DMRG, a two-dimensional system must be mapped to a one-dimensional lattice topology due to the nature of the MPS, which must then be optimized by sweeping through the system in a “snake-like” manner [22]. Thus, local interactions become nonlocal with respect to the MPS, and an efficient representation of a locally entangled two-dimensional state becomes impossible. An overview of recent state-of-the-art results on the two-dimensional Hubbard model calculated using a variety of numerical algorithms has been given in a recent review [2]. One interesting conclusion is that, in spite of the limitations of MPS-based methods for two-dimensional systems, competitively accurate results have been obtained for two-dimensional frustrated spin systems using the DMRG. For example, for the Heisenberg model on the kagome lattice, DMRG calculations yield results that have among the best levels of variational accuracy [23, 24] and are in excellent agreement with results from MERA [25] and PEPS [26].

The amount of entanglement present when partitioning a system, however, is basis dependent [9, 27, 28].

Therefore, a given problem could possibly be solved with significantly less computational cost if an optimal representation could be found [29, 30]. For example, the DMRG treatment of a two-dimensional noninteracting fermionic problem is exponentially difficult in real space due to the high level of entanglement, whereas in a momentum-space representation the solution is a simple product state, which can be represented exactly with a low-dimensional MPS [27]. For the case of non-vanishing interactions, however, interactions that are local in a particular basis (typically real space) become nonlocal after a change of basis, influencing the scaling behavior of entanglement with system size dramatically. For systems with sufficient locality, i.e., with hopping and interaction terms that have a finite range within a lattice of a particular dimensionality, the scaling of the entropy for ground and certain low-lying excited states is thought to obey the entropy area law [31]. Thus, such models with short-range interactions can, generically, be simulated efficiently using tensor network state algorithms. When locality is lost, the area law, in general, can break down, making efficient treatment of the problem difficult [32]. Nevertheless, for small interaction strengths and for a given error threshold, it is still potentially possible to find a representation that is computationally more efficient for particular system sizes. In addition, the weak-coupling regime is often well approximated by analytical approaches [33], providing connections between numerical and analytical results. Furthermore, geometrical aspects of a Hamiltonian in a particular representation can have a more compact description in another representation; in particular, what is long range in real space tends to be short range in momentum space and vice versa.

Motivated by the arguments above, here we study and compare the real-space and momentum-space representations of the Hubbard model in one and two dimensions from the point of view of quantum information entropies. Although previous numerical studies of the Hubbard model using the momentum-space DMRG method (k-DMRG) date from as long as two decades ago [27, 34, 35], these studies were severely limited in the number of block states kept, worked with non-optimally ordered MPSs for the two-dimensional system, and did not study the behavior of quantum-information-based quantities. Therefore, a rigorous analysis of the scaling of the entanglement entropy and other measures of quantum correlation as a function of system sizes and interaction strengths could not be carried out. In this paper, we reexamine the Hubbard model using the k-DMRG, presenting state-of-the-art results using a modern MPS-based DMRG code that optimizes the mapping of the lattice to an MPS and can keep up to the order of 50 000 block states for the momentum-space Hubbard model. To study the intrinsic properties of the MPS representation, we carry out a detailed analysis of entanglement scaling with system size and interaction strength U in one and two dimensions.

Our study is also motivated by the fact that information on the dimensionality and geometry of the lattice

as well as range of the hopping is encoded in the kinetic term, which is diagonal in momentum space. Thus, the k-DMRG is less sensitive than the real-space representation to changes in these aspects of the model, that is, more complex cases that add computational cost in real space could potentially be treated with little additional cost in momentum space; it is important to determine to what extent this is the case. Furthermore, the momentum-space representation is intrinsically translationally invariant, so that finite-size corrections can be treated by scaling systems with periodic and antiperiodic boundary conditions rather than the open boundary conditions that must usually be used in real space. Finally, using the k-DMRG the entanglement patterns of the wave function can be analyzed with respect to momentum, allowing us to make connections between weak-coupling analytic pictures [33] and numerical results. In particular, we will be able to study the role of umklapp in one dimension and the effect of perfect and non-perfect nesting in two dimensions.

The paper is organized as follows. In Sec. II, we describe the model, define the quantum-information-based quantities that we treat, and describe the numerical methods. In Sec. III, we apply our approach to the one- and two-dimensional Hubbard models in momentum space. Finally, Sec. IV contains our conclusions.

II. MODEL AND METHODS

A. Hubbard model

The Hamiltonian of the Hubbard model in real space has the form

$$H = -t \sum_{\langle \mathbf{r}, \mathbf{r}' \rangle, \sigma} \left(c_{\mathbf{r}\sigma}^\dagger c_{\mathbf{r}'\sigma} + \text{H.c.} \right) + U \sum_{\mathbf{r}} n_{\mathbf{r}\uparrow} n_{\mathbf{r}\downarrow}, \quad (1)$$

where $c_{\mathbf{r}\sigma}^\dagger$ and $c_{\mathbf{r}\sigma}$ creates and annihilates a particle on site \mathbf{r} with spin $\sigma = \{\downarrow, \uparrow\}$, $n_{\mathbf{r}\sigma} = c_{\mathbf{r}\sigma}^\dagger c_{\mathbf{r}\sigma}$ measures the number of electrons on site \mathbf{r} with spin σ , and $\langle \mathbf{r}, \mathbf{r}' \rangle$ denotes a nearest-neighbor pair on sites \mathbf{r} and \mathbf{r}' . The dimensionality and structure of the lattice is contained in the definition of the index \mathbf{r} and in the definition of the nearest neighbors. By carrying out a change of basis using a Fourier transformation, i.e., $c_{\mathbf{k}\sigma} = 1/\sqrt{N} \sum_{\mathbf{r}} \exp(i\mathbf{k} \cdot \mathbf{r}) c_{\mathbf{r}\sigma}$, we obtain the corresponding momentum-space Hamiltonian

$$H = \sum_{\mathbf{k}\sigma} \varepsilon(\mathbf{k}) c_{\mathbf{k}\sigma}^\dagger c_{\mathbf{k}\sigma} + \frac{U}{N} \sum_{\mathbf{k}p\mathbf{q}} c_{\mathbf{p}-\mathbf{q}\uparrow}^\dagger c_{\mathbf{k}+\mathbf{q}\downarrow}^\dagger c_{\mathbf{k}\downarrow} c_{\mathbf{p}\uparrow}, \quad (2)$$

if periodic boundary conditions are applied, where $c_{\mathbf{k}\sigma}^\dagger$ and $c_{\mathbf{k}\sigma}$ creates and annihilates a particle with momentum \mathbf{k} , with \mathbf{k} a vector with the dimensionality of the lattice, and N is the number of sites. In one dimension, $\mathbf{k} = k = (2\pi n)/N$, with $-N/2 < n \leq N/2$ and

$\varepsilon(k) = -2t \cos(k)$. In two dimensions, $\mathbf{k} = (k_x, k_y)$ and $\varepsilon(\mathbf{k}) = -2t \cos(k_x) - 2t \cos(k_y)$. Note that the \mathbf{k} points will be shifted by a half-interval if antiperiodic rather than periodic boundary conditions are applied in a particular direction. Due to momentum conservation, the total momentum before and after the scattering processes given by the four-operator term is the same. The interaction strength U is given in units of t with $t = 1$.

In the remainder of the paper, we will use the expression ‘‘Hartree-Fock orbitals’’ to denote single-particle orbitals, i.e., \mathbf{k} points, that are filled for the noninteracting case, $U = 0$. These points will be within the Fermi surface where the ‘‘Fermi surface’’ is defined by the boundary in momentum space between occupied and unoccupied points for $U = 0$. In one dimension, the Fermi surface consists of two points, $\pm k_F$, and in two dimensions, it forms a curve or set of curves in the k_x - k_y plane in the infinite-system limit. Also note that we measure distance in momentum space in units of the unit vectors of the reciprocal space, that is, $2\pi/N$ for the one-dimensional chain and $2\pi/L_x$ or $2\pi/L_y$ for the two-dimensional square lattice of dimension $L_x \times L_y = N$. Use of terms such as ‘‘long range’’ or ‘‘short range’’ as applied to momentum space will refer to momentum-space distances measured in these units. ‘‘Volume’’ in momentum space will be shorthand for the number of discrete momentum points in a momentum region or in the entire lattice.

B. DMRG and entanglement-based measures

In the two-site DMRG, the full Hilbert space of a finite system consisting of N sites, $\Lambda^{(N)} = \otimes_{i=1}^N \Lambda_i$, is approximated by a tensor product of four tensor spaces, $\Xi_{\text{DMRG}}^{(N)} = \Xi^{(l)} \otimes \Lambda_{l+1} \otimes \Lambda_{l+2} \otimes \Xi^{(r)}$. The basis states of Λ_i , the local-site (tensor) space, depend on the representation in which the Hamiltonian is formulated. The bases of the $\Xi^{(l)}$ and $\Xi^{(r)}$ are formed through a series of unitary transformations generated by singular value decompositions (SVD) applied repeatedly as the bipartite partition of the system is moved back and forth through the lattice (‘‘sweeping’’). Thus, their actual form depends on the details of the procedure [28, 36–39]. The nature and size of the bases of $\Xi^{(l)}$ and $\Xi^{(r)}$ can be optimized using the concepts of quantum information theory [40–42] i.e., by controlling the level of entanglement [31, 43, 44] of the subsystems [9, 27, 28, 45–47]. Therefore, a given problem can be solved with significantly less computational resources if an optimal representation is found [29, 30, 47, 48].

The single-site von Neumann entropy, $s_i = -\text{Tr} \rho_i \ln \rho_i$ is formed from the reduced density matrix ρ_i of the subsystem consisting of the site i . Its value ranges from 0 to $\ln 4$ for a fermionic site with spin, with larger values corresponding to a more mixed state and a larger contribution to the correlation energy. In fact, an exact expression for the local single-site entropy in the ground state of the one-dimensional Hubbard model has also

been derived [49]. Similarly, the two-site von Neumann entropy can be constructed using the reduced density matrix of a subsystem built from orbitals i and j , ρ_{ij} . The mutual information $I_{ij} = s_i + s_j - s_{ij}$ describes how these two orbitals are correlated with each other given that they are embedded in the whole system. It includes contributions from correlations of both classical and quantum nature [50]. The number of block states, $M_l = \dim \Xi^{(l)}$ and $M_r = \dim \Xi^{(r)}$, required to achieve a given convergence is determined by the von Neumann entropy of segments of length $l = 1 \dots N - 1$ of the finite chain (‘‘blocks’’) [45, 46]. In practice, we fix the accuracy threshold and vary the number of block states $M_{\text{max}} = \max(M_l, M_r)$ to maintain the threshold. The l -site block entropy $S(l)$ can be used to study critical and gapped phases and is an easily accessed quantity numerically, as the reduced density matrices ρ_l are generated automatically within the DMRG procedure.

Ground states of lattice models with local interactions are thought to obey the so-called entropy area law relatively generically [31]. In one dimension, the block entropy can be shown to saturate with block length for gapped models and to diverge logarithmically for critical systems [45]. In two dimensions, the entropy area law still applies if interactions are short-range and all correlation functions have finite correlation lengths [51]. When nonlocal interactions are present, the arguments for the applicability of the area law break down. In nonlocal models, the profile of the block entropy has a more general form that depends on several factors, as has been discussed for the Hubbard model in momentum space [27], for the XXZ chain in momentum space [52], and for quantum chemical systems [53]. The block entropy profile can be optimized by minimizing the entanglement distance, defined as

$$I_{\text{dist}} = \sum_{ij} I_{ij} d^\eta, \quad (3)$$

where the sum is weighted by the η^{th} moment of the distance ($\eta \geq 1$) [29, 47, 53], and the distance function d depends on the tensor network topology [54]. In the MPS-based DMRG, $d = |i - j|$ refers to the distance between sites within the MPS chain, and Eq. (3) can be minimized by permuting the lattice sites, i.e., by reordering [27, 47, 53]. In this way, both the sum of $S(l)$ over $l = 1 \dots N - 1$ and the maximum of $S(l)$ over all l , $\max[S(l)]$, can be reduced significantly. The sum is related to the computational time of a full sweep, and the maximum determines the maximum amount of computational resources required for one DMRG step. By changing a local hopping to a nonlocal hopping by permuting the ordering of lattice sites, one can interpolate between a logarithmic- (area law) and a linear (volume law) scaling [55], as has been demonstrated in a study of the one-dimensional Hubbard model [32].

Another way of reducing I_{dist} is to transform the single-particle basis, choosing the transformation to optimize

entanglement measures [27, 30, 48]. For example, for the noninteracting ($U = 0$) Hubbard model, the Hamiltonian is diagonal in the momentum-space representation, $s_i = 0$, $I_{i,j} = 0$, and the ground state is a product state; thus, I_{dist} and $S(l)$ are zero. On the other hand, for finite Coulomb interaction U , these quantities become finite and, in the $U \rightarrow \infty$ limit, $s_i = \ln 4$, i.e., all sites are in maximally mixed states. Therefore, the momentum-space representation is expected to be useful in a regime adiabatically connected to the free-particle case, typically the weak-coupling regime.

Entanglement analysis is also a very powerful tool to obtain physical information encoded in the wave function [29, 56–59]. Entanglement patterns by the two-site mutual information provide information about the overall correlations in the system, while the generalized correlation functions used to form the two-site reduced density matrix can be used to identify dominant correlations. For more detailed discussions, see Refs. 47 and 59.

C. Momentum-space DMRG implementation

Some aspects of the usual DMRG algorithm must be adapted to obtain an efficient implementation for momentum-space Hamiltonians.

The main difficulty in implementing the momentum-space DMRG comes from the fact that short-range interaction terms such as that in the real-space Hubbard model, Eq. (1), become long-range in the momentum basis. Naively implemented, the momentum-space Hubbard model Hamiltonian requires the calculation of $\mathcal{O}(N^3)$ terms in order to apply the interaction part of the Hamiltonian to the wave vector because of sum over three momenta in Eq. (2). In an MPS formulation, the matrix product operator (MPO) would have bond dimension $M \propto N^3$, resulting in unacceptable resource requirements even for relatively small system sizes. This problem can be ameliorated by factorizing the Hamiltonian and building partial sums over certain combinations of operators within the left and right DMRG blocks, resulting in an effective one-index sum and a computational cost per diagonalization step of $\mathcal{O}(N)$. At the same time, the required composed operators must be saved and updated iteratively, resulting in additional memory cost of $\mathcal{O}(N)$. While this technique was already described and used in the first work on momentum-space DMRG [34], here we have adapted this method to the MPS framework and optimized it within this framework.

The factorization described above can only be carried out for particular forms of the interaction of which the Fourier-transformed on-site interaction is one. The CPU time and memory costs for a single diagonalization step can be reduced to $\mathcal{O}(N)$, compared to $\mathcal{O}(N^2)$ for other more general long-range Hamiltonians (e.g., those for quantum chemistry) [60]. Certain extensions to the Hubbard interaction, such as nearest- or next-nearest-neighbor repulsion can also be factorized to obtain $\mathcal{O}(N)$

terms, only affecting the prefactor but not the scaling in the computational cost [34]. In contrast to the real-space case, adding longer-range terms to the hopping in momentum space only affects the dispersion relation, which enters the Hamiltonian as a diagonal term, and therefore does not change the MPO bond dimension.

One significant advantage of working in the momentum-space representation is the availability of the additional momentum quantum numbers. Within an MPS-based DMRG implementation, all contractions of the tensor network can be reduced to a series of matrix operations, principally multiplications. The Abelian momentum quantum numbers can be used to decompose all matrices to block form, where the blocks are labeled by quantum number pairs. Carrying out operations only using these blocks significantly speeds up the algorithm and significantly lowers the memory required. For the Hubbard model calculations carried out here, we typically obtain very small dense blocks with $\mathcal{O}(10 \times 10)$ elements, which make up sparse matrices with up to millions of blocks. This large number of blocks makes it essential to carry out the quantum-number bookkeeping as efficiently as possible and to reduce additional overhead to a minimum. In our code, we obtain very good results by using hash tables to do the quantum-number bookkeeping.

At the same time, use of the momentum quantum numbers introduces convergence problems because the quantum numbers of local states of two neighboring sites can, in general, no longer be recombined to the same target quantum number in more than one way. Due to this, the algorithm tends to get stuck in local minima even if the DMRG is implemented in the usual way with two single sites in the center. (Such problems typically occur in the variant of the DMRG where a single site is taken in the center.) For example, a two-site k-DMRG calculation initialized with a product state will remain stuck in that state throughout the entire calculation unless additional measures are taken. For the single-site real-space DMRG algorithm, an effective solution to this problem is to add a noise term to the density matrix [61]. Here, we add such a noise term within the two-site algorithm and find that the convergence problem is essentially eliminated, provided that the noise term is given appropriate strength.

In our implementation, which exploits the additional momentum quantum numbers and carries out an efficient factorization of the interaction term, a comparatively large number of block states can be kept at reasonable computational cost. We typically increase the number of block states after every second full sweep by 4 000 states and keep a maximum of up to 54 000 states during the last two sweeps. Running on 10 CPU cores (Intel[®] Xeon[®] 5140), the calculation for a 6×6 -site system with a maximum of 54 000 states kept during the last two sweeps takes roughly three days of wall-clock time and uses 30 GB of main memory. We use two codes, one sequential code based on a strongly modified version of

the open-source ITensor library [62] and one parallelized code based on a self-written tensor library.

In addition to these technical optimizations, choosing appropriate boundary conditions for each calculation so that a “closed-shell” configuration is obtained for the Fermi sea can lower the maximum block entropy and thus improve the DMRG convergence for a fixed number of block states. The idea is to coordinate lattice size, filling, and boundary conditions so that the noninteracting ground state is non degenerate. For example, consider the noninteracting half-filled one-dimensional Hubbard model in momentum space. For periodic boundary conditions and system sizes $N \in \{2, 6, 10, 14, \dots\}$ the ground state in momentum space is a unique product state, while system sizes $N \in \{4, 8, 12, 16, \dots\}$ lead to a fourfold-degenerate ground state. For antiperiodic boundary conditions, the momentum-space sites are shifted, reversing the situation. It is known that this behavior is preserved in the exact Bethe ansatz solution for the interacting one-dimensional system [63]. Although interaction tends to wash out degeneracies in open-shell configurations, taking closed-shell configurations for weak to moderate coupling strength is still very useful. For moderate coupling strength, closed-shell configurations have a unique Hartree-Fock ground state and thus have fewer energetically low-lying excitations, leading to a less entangled ground state. The system sizes, fillings, and boundary conditions in the next section are selected accordingly.

III. RESULTS

In this section, we present our numerical results obtained with the momentum-space DMRG on the half-filled and doped Hubbard model in one and two dimensions for finite systems. First, we analyze the entanglement patterns in the ground-state wave function, identifying relevant correlations by examining highly entangled momenta points. Next, we calculate the wave-function coefficients in full tensor form, which are an alternate way of characterizing the wave function and can be connected to the configuration-interaction (CI) expansion technique used in quantum chemistry. Finally, we study the scaling of entanglement, quantified by the von Neumann block entropy, as a function of interaction strength and system size.

A. Entanglement patterns and correlations

In order to investigate the entanglement structure and optimize the site ordering within the MPS, we examine the two-site mutual information I_{ij} as well as the site occupancy and single-site entropy for the one- and two-dimensional Hubbard models.

We start with the half-filled one-dimensional case in Fig. 1. Figure 1(a) is a (color) density plot of the I_{ij} matrix, with the row and column indices i and j referring to

the sites of the DMRG chain, while in Fig. 1(b) the same correlations are plotted as lines between the corresponding points in momentum space, where the momentum points are arranged in the vertical direction according to the dispersion relation $\varepsilon(k)$. One can see that the pairs of sites with the strongest correlations are the pairs which are associated with the allowed scattering processes close to the Fermi surface, as depicted in Fig. 2. Consequently, the single-site entropy s_i [Fig. 1(d)] shows two peaks at the Fermi points. Correspondingly, the site occupancy [Fig. 1(c)] drops from close to 2.0 to almost 0.0 at the Fermi points; the sharp drop is characteristic of the relatively weak interaction strength $U = 1.0$. The strongest bonds can be found between those pairs of sites with distance $k_1 - k_2 = \pi$ in momentum space. Therefore, in order to improve the DMRG convergence, sites with a separation π in momentum space should be placed on neighboring sites on the DMRG chain. In addition, pairs close to the Fermi surface should be put in the center of the DMRG chain. Automatic ordering of the sites, carried out by minimizing the entanglement distance (3), gives the optimal ordering shown in Table I, which corresponds quite well to these heuristic rules.

We now examine the doped one-dimensional system [Fig. 3], taking an average particle number $n = 0.727$. The entanglement structure is similar to that in the half-filled case; the pairs of sites close to and symmetric relative to the Fermi points (now at somewhat smaller k) show the strongest correlations [see Fig. 3(b)]. However, the pairs of momentum points analogous to those which, in the half-filled case, are associated with backward and umklapp scattering, g_1 and g_3 , respectively, are now significantly less correlated. This can be understood by examining the effect of the shifting of the Fermi points on the conservation of momentum. In the half-filled case, the energetically lowest excitations relative to the Hartree-Fock ground state $|\Psi\rangle_{\text{HF}}$ that have the same total momentum are of four different types:

$$|\Psi\rangle_A = c_{\pm k_2 \downarrow}^\dagger c_{\pm k_2 \uparrow}^\dagger c_{\mp k_1 \uparrow} c_{\mp k_1 \downarrow} |\Psi\rangle_{\text{HF}}, \quad (4a)$$

$$|\Psi\rangle_B = c_{k_2 \sigma}^\dagger c_{-k_2 \bar{\sigma}}^\dagger c_{k_1 \sigma} c_{-k_1 \bar{\sigma}} |\Psi\rangle_{\text{HF}}, \quad (4b)$$

$$|\Psi\rangle_C = c_{k_2 \sigma}^\dagger c_{-k_2 \bar{\sigma}}^\dagger c_{k_1 \bar{\sigma}} c_{-k_1 \sigma} |\Psi\rangle_{\text{HF}}, \quad (4c)$$

and

$$|\Psi\rangle_D = c_{k_2 \sigma}^\dagger c_{-k_2 \sigma}^\dagger c_{k_1 \sigma} c_{-k_1 \sigma} |\Psi\rangle_{\text{HF}}, \quad (4d)$$

with $k_1 = k_F - \delta_k$, $k_2 = k_F + \delta_k$, $\delta k = \pi/N$, and $\sigma \in \{\uparrow, \downarrow\}$. In the doped case, states of type A no longer have the same momentum as $|\Psi\rangle_{\text{HF}}$ because $k_F \neq \pi/2$. Thus, they cannot be in the space of the ground state. Without these excitations, two-particle umklapp processes symmetric to the Fermi surface are no longer possible; this also holds for higher excitations. In terms of equal-time correlations, the number of excitations that make up the interacting ground state and can contribute to the correlations drops, consequently lowering the two-

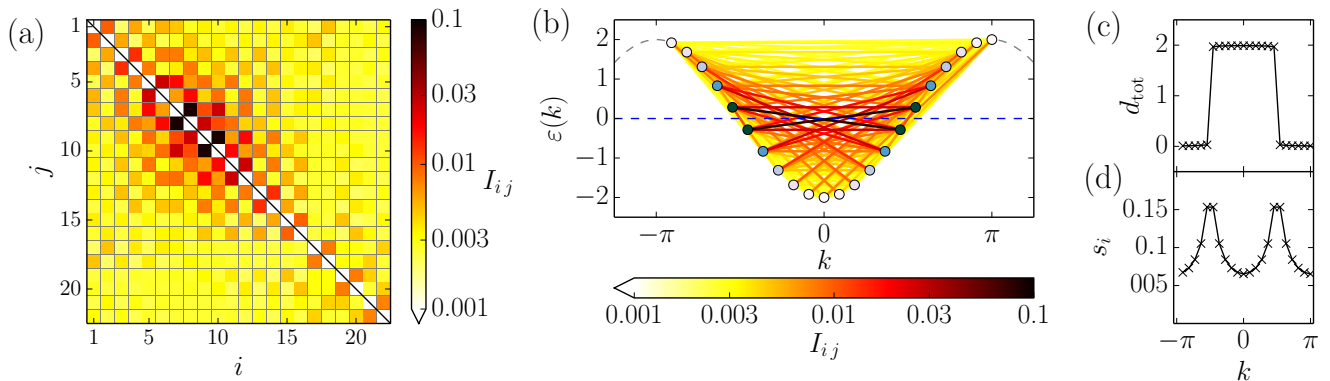


FIG. 1. (Color online) Ground state of the $N = 22$ -site Hubbard model in momentum space (with periodic boundary conditions) for $U = 1.0$ at half-filling. (a) Two-site mutual information $I_{i,j}$ between MPS sites i and j for the optimal site ordering (Table I). (b) Two-site mutual information $I_{i,j}$ between momentum points k , where the k points are arranged according to the dispersion relation. The blue (gray) dashed line indicates the Fermi level. (c) Site occupancy d_{tot} . (d) Single-site entropy s_i .

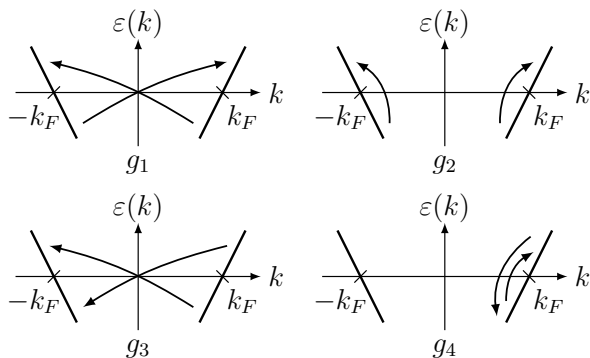


FIG. 2. Scattering processes near the Fermi surface in the half-filled system where g_1 is backward scattering, g_2 and g_4 forward scattering, and g_3 umklapp scattering.

site mutual information between these sites.

In matrix form for optimal ordering, I_{ij} [Fig. 3(a)] is somewhat less diagonal-dominated than at half-filling, but the strongly off-diagonal elements have comparable or smaller values than the half-filled case. Note that although the Fermi edge is quite sharp [Fig. 3(c)] the peaks in the single-site entropy s_i [Fig. 3(d)] are somewhat washed out relative to the half-filled case, reflecting the reduced entanglement of momenta near the Fermi points.

We now proceed to the entanglement patterns in the two-dimensional Hubbard model. Many characteristics observed in the one-dimensional model can be found in generalized form in the two-dimensional case. At half-filling, we consider points \mathbf{k}_F and $\tilde{\mathbf{k}}_F$ that lie on opposite sides of the Fermi surface, i.e., that fulfill the nesting condition $\mathbf{k}_F = \tilde{\mathbf{k}}_F + (\pi, \pi)$. Pairs of lattice sites directly above and below such opposing locations on the Fermi surface also fulfill the nesting condition and allow for energetically favorable processes that are generalizations of

i	n=1.0		n=0.727	
	k	$\epsilon(k)$	k	$\epsilon(k)$
1	9	1.683	10	1.819
2	20	-1.683	13	1.819
3	8	1.31	14	1.511
4	19	-1.31	9	1.511
5	7	0.831	8	1.081
6	18	-0.831	15	1.081
7	17	-0.285	1	-1.98
8	6	0.285	0	-1.98
9	16	0.285	2	-1.819
10	5	-0.285	21	-1.819
11	15	0.831	4	-1.081
12	4	-0.831	18	-0.564
13	14	1.31	5	-0.564
14	3	-1.31	19	-1.081
15	13	1.683	20	-1.511
16	2	-1.683	3	-1.511
17	10	1.919	17	0.0
18	21	-1.919	6	0.0
19	1	-1.919	7	0.564
20	12	1.919	16	0.564
21	11	2.0	11	1.98
22	0	-2.0	12	1.98

TABLE I. Mapping between MPS-site indices i and momentum-space site indices k for the optimal ordering of the of the 22-site system depicted in Figs. 1 and 3, with momentum points $k = k \frac{2\pi}{22}$ for half-filling $n = 1.0$ and shifted momentum points $k = (k + 0.5) \frac{2\pi}{22}$ for the doped case $n = 0.727$.

umklapp processes in the one-dimensional system. As can be seen in Figs. 4(a) and (b), such pairs of points have particularly large values of I_{ij} , with the largest occurring for pairs of points near the corners of the Fermi surface, i.e., the pairs $\mathbf{k} = (\pm\delta k_x, \pi)$ and $\tilde{\mathbf{k}} = (\pi \pm \delta k_x, 0)$, with $\delta k_x = \pi/L_x$. Note that there is asymmetry in the k_x - k_y plane due to the mixed boundary conditions (periodic in y and antiperiodic in x). The single-site entropy [Fig. 4(d)] reflects this structure in that the largest val-

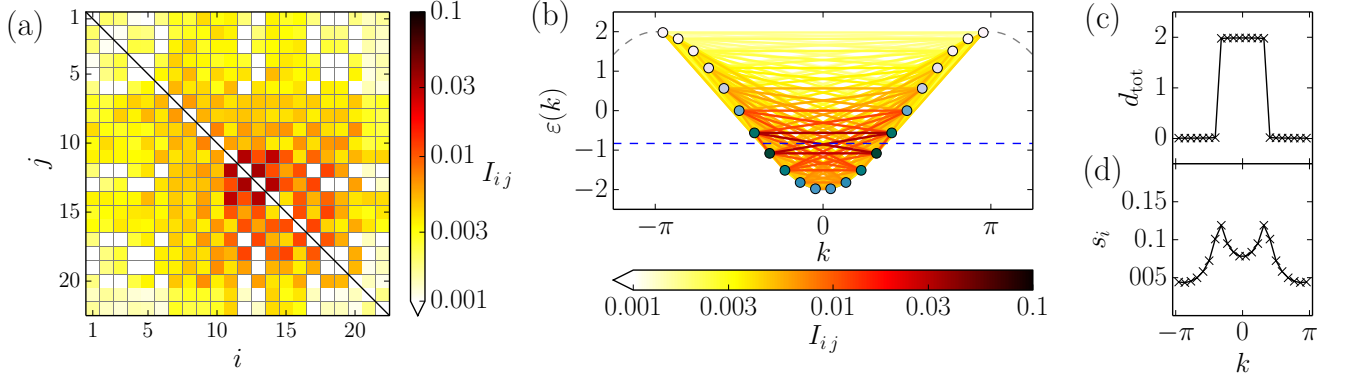


FIG. 3. (Color online) Ground state of the doped $N = 22$ -site Hubbard model in momentum space (with antiperiodic boundary conditions) for $U = 1.0$ at average occupancy $n = 0.727$. (a) Two-site mutual information $I_{i,j}$ between MPS sites i and j for the optimal site ordering (Table I). (b) Two-site mutual information $I_{i,j}$ between momentum points k , where the k points are arranged according to the dispersion relation. The (blue) dashed line indicates the Fermi level. (c) Site occupancy d_{tot} . (d) Single-site entropy s_i .

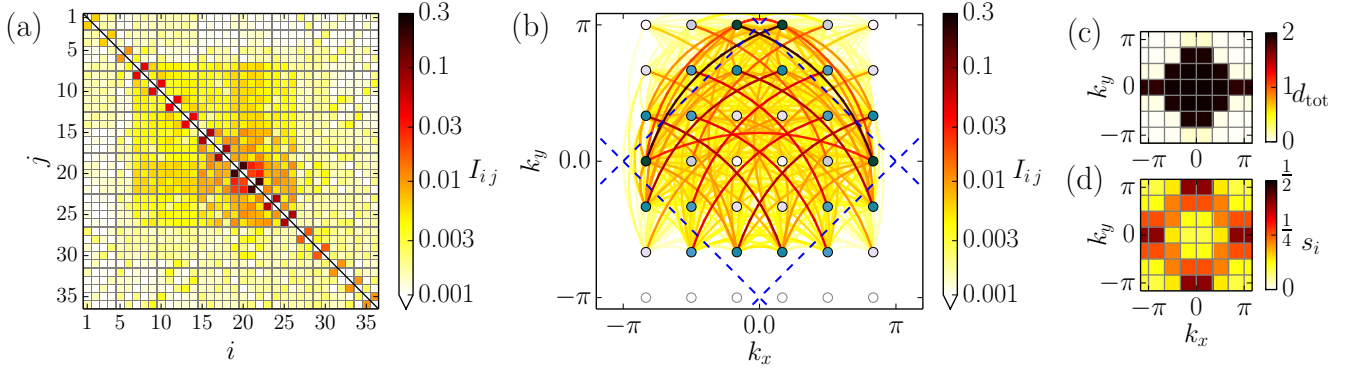


FIG. 4. (Color online) Ground state of the 6×6 Hubbard model in momentum space (antiperiodic / periodic boundary conditions in x - / y -direction) for $U = 2.0$ at half-filling: (a) two-site mutual information $I_{i,j}$ between MPS sites i and j for the optimal site ordering (Table II). (b) two-site mutual information $I_{i,j}$ between momentum points (k_x, k_y) . The (blue) dashed line indicates the Fermi surface. (c) Site occupancy d_{tot} . (d) Single-site entropy s_i .

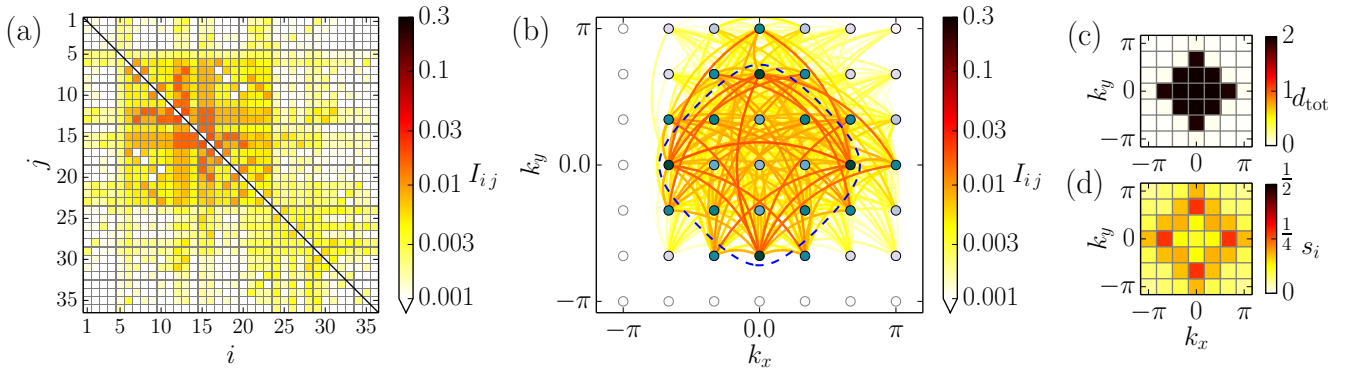


FIG. 5. (Color online) Ground state of the doped 6×6 Hubbard model in momentum space (periodic boundary conditions in both directions) for $U = 2.0$ at $n = 0.722$ filling: (a) two-site mutual information $I_{i,j}$ between MPS sites i and j for the optimal site ordering (Table II). (b) two-site mutual information $I_{i,j}$ between momentum points (k_x, k_y) . The (blue) dashed curve indicates the Fermi surface. (c) Site occupancy d_{tot} . (d) Single-site entropy s_i .

i	n=1.0			n=0.722		
	k_x	k_y	$\epsilon(\mathbf{k})$	k_x	k_y	$\epsilon(\mathbf{k})$
1	2	3	3.732	3	2	3.0
2	5	0	-3.732	3	4	3.0
3	3	3	3.732	2	3	3.0
4	0	0	-3.732	4	3	3.0
5	2	2	2.732	0	0	-4.0
6	5	5	-2.732	5	5	-2.0
7	1	2	1.0	2	1	0.0
8	4	5	-1.0	4	5	0.0
9	4	4	1.0	2	5	0.0
10	1	1	-1.0	4	1	0.0
11	4	2	1.0	3	0	0.0
12	1	5	-1.0	0	2	-1.0
13	1	4	1.0	0	4	-1.0
14	4	1	-1.0	0	3	0.0
15	3	1	0.732	2	0	-1.0
16	0	4	-0.732	4	0	-1.0
17	5	4	-0.732	1	2	0.0
18	2	1	0.732	5	4	0.0
19	2	0	-0.268	5	2	0.0
20	5	3	0.268	1	4	0.0
21	3	0	-0.268	1	1	-2.0
22	0	3	0.268	5	1	-2.0
23	2	5	0.732	1	5	-2.0
24	5	2	-0.732	1	0	-3.0
25	3	5	0.732	5	3	1.0
26	0	2	-0.732	5	0	-3.0
27	4	0	-2.0	1	3	1.0
28	1	3	2.0	0	1	-3.0
29	4	3	2.0	0	5	-3.0
30	1	0	-2.0	3	1	1.0
31	3	2	2.732	3	5	1.0
32	0	5	-2.732	4	2	2.0
33	2	4	2.732	2	4	2.0
34	5	1	-2.732	4	4	2.0
35	3	4	2.732	2	2	2.0
36	0	1	-2.732	3	3	4.0

TABLE II. Mapping between and MPS-site indices i and momentum-space indices $\{k_x, k_y\}$ for the optimal ordering of the 6×6 system depicted in Figs. 4 and 5, with momentum points $(k_x, k_y) = ((k_x + 0.5)\frac{2\pi}{6}, k_y\frac{2\pi}{6})$ for half-filling $n = 1.0$ and $(k_x, k_y) = (k_x\frac{2\pi}{6}, k_y\frac{2\pi}{6})$ for the doped case, $n = 0.722$.

ues occur at the $\mathbf{k} = (\pm\pi, 0)$ and $\mathbf{k} = (0, \pm\pi)$ corners of the Brillouin zone. As can be seen in Fig. 4(a), I_{ij} has a fairly diagonal structure for the optimal ordering, except for a relatively limited region in the middle of the MPS site ordering. However, this region is quite important for the convergence in that the DMRG steps with a high number of states kept will be required in this region.

Doping the two-dimensional system deforms the Fermi surface and destroys its perfect nesting, as is depicted in Fig. 5(b). The sites that correspond to those that showed the strongest correlations in the half-filled case are now less correlated. Similarly to the one-dimensional case, reordering the MPS sites can significantly reduce the entanglement in the system, but a “perfect” ordering is again not possible because of loops in the entangle-

ment structure, which can be seen in Figs. 4(b) and 5(b). The site occupancy [Fig. 5(c)] shows a sharp jump at the Fermi surface, and the single-site entropy [Fig. 5(c)] a relatively broad peak, with the highest values occurring at the corners of the Fermi surface, in the $(k_x, 0)$ and $(0, k_y)$ directions.

The mappings between MPS sites i and momentum points k / \mathbf{k} for optimal ordering for the one-dimensional systems depicted in Figs. 1 and 3 are listed in Table I, and the two-dimensional systems depicted in Figs. 4 and 5 in Table II. In the matrix plots of I_{ij} [Figs. 1(a), 3(a), 4(a), and 5(a)], the first minor diagonals correspond to the correlation between neighboring sites, the second minor diagonals to correlations between next-nearest neighbors, etc. Therefore, the task of optimizing the MPS ordering can be graphically interpreted as permuting the columns and rows of I_{ij} symmetrically with the purpose of arranging its entries in descending order from the main diagonal I_{ii} towards the outer edges I_{1N} and I_{N1} .

The decay rate of the elements of I_{ij} , provides important information about the correlations in the system [59]. This decay is depicted on a logarithmic scale in descending order for the 6×6 Hubbard model in Fig. 6, for both the half-filled and doped systems at two different U values. As can be seen, there are plateaus with jumps and changes in slope in all four curves. Adopting the terminology of quantum chemistry, the small number of components with large I_{ij} values are associated with the so-called static correlations, while the large number of elements with small weight correspond to dynamic correlations. As the interaction strength U is increased, the curves shift upward for both the half-filled and doped cases, indicating an increased level of entanglement. For the doped case, the static correlations are significantly smaller than for the half-filled case. This is due to the absence of the umklapp processes in the doped case. Thus, we expect that the doped case can be studied more efficiently in momentum-space representation than the half-filled case. Note that in real space the opposite holds.

We have also calculated the correlation patterns and the decay of the two-site mutual information for the 6×6 lattice at interaction strength $U = 4.0$. While the results do not reveal qualitatively new behavior, the DMRG convergence becomes critical due to the increased overall entanglement in the system. Compared to $U = 2.0$, the correlations between sites that fulfill the nesting condition in the half-filled case become even more dominant.

B. Wave-function coefficients

The wave-function coefficients $\Psi(\sigma_1, \dots, \sigma_N)$ in the full tensor representation $\Psi = \sum_{\{\sigma_1, \dots, \sigma_N\}} \Psi(\sigma_1, \dots, \sigma_N) |\sigma_1, \dots, \sigma_N\rangle$ can also be calculated from the DMRG wave function within the MPS formalism. The squares of the coefficients $\Psi(\sigma_1, \dots, \sigma_N)$ of the ground state of the half-filled 4×4 Hubbard model in momentum space are shown in Fig. 7(b) for different

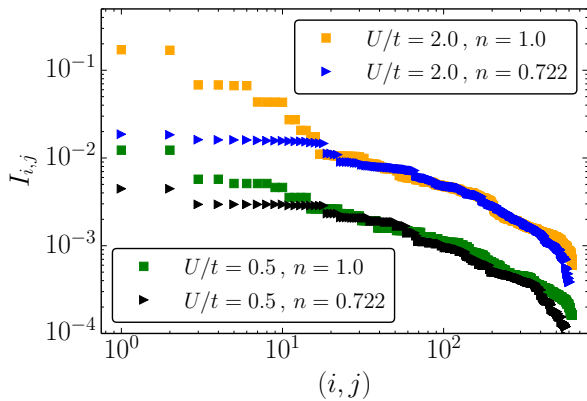


FIG. 6. (Color online) Two-site mutual information $I_{i,j}$ for the ground state of the 6×6 Hubbard model in momentum space for different U values and different fillings n . The values are sorted in descending order. We include only unique entries of $I_{i,j}$, i.e., take $i > j$.

values of U . The increased level of entanglement is reflected by the increase in the weight of the wave function coefficients, a behavior similar to that seen for the decay of I_{ij} in Fig. 6.

In order to make contact with the CI-expansion technique used in quantum chemistry, the number of excitations from the Hartree-Fock state (CI = 0) in the corresponding basis states $|\sigma_1, \dots, \sigma_N\rangle$ for $U = 2.0$ are shown in Fig. 7(a). The single CI (CI = 1) and the second highest (CI = $N - 1$) excitation are forbidden due to momentum conservation. The most important excitations are the double, triple, and quadruple CI determinants, but higher CI excitations also provide significant contributions. For small U values, these excitations are reflected in the behavior of the square of the coefficients of the wave function in that there are plateaus with jumps. The first few plateaus come mainly from the lower-order CI excitations. This structure becomes smoother for larger interaction strength and completely disappears for large U values. The decay of the coefficients with coefficient index also becomes increasingly longer range with increasing U . Therefore, a truncated CI expansion would not converge sufficiently rapidly in the level of excitation in the momentum-space representation due to strong correlations in the system, except possibly at very small U values.

C. Block entropy and entanglement scaling

After studying the entanglement patterns and correlations for particular finite-sized systems, we now analyze the scaling of the entanglement as a function of interaction strength and system size. We begin by examining the behavior of lattice-site-dependent quantities at optimal ordering (i.e., as a function of the DMRG index i) for the two-dimensional system, for which the behav-

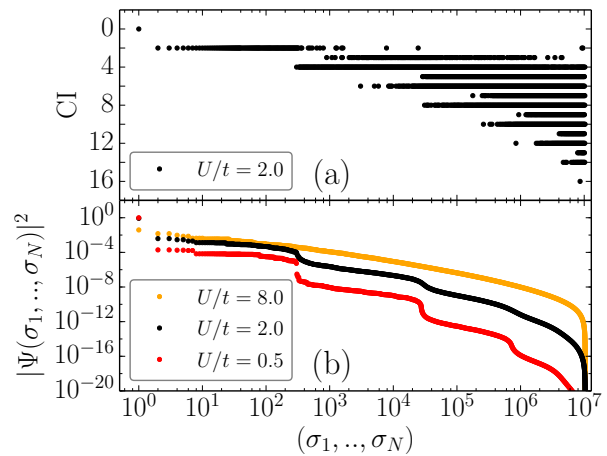


FIG. 7. (Color online) (a) Number of excitations from the Hartree-Fock state in the basis states $|\sigma_1, \dots, \sigma_N\rangle$ for $U = 2.0$. (b) Square of the coefficients $|\Psi(\sigma_1, \dots, \sigma_N)|^2$ of the ground state of the 4×4 Hubbard model in momentum space at half-filling for different values of U . The data in (a) and (b) is sorted by the value of $|\Psi(\sigma_1, \dots, \sigma_N)|^2$ in descending order.

ior is not known and is particularly interesting in view of the nontrivial mapping of the two-dimensional momentum lattice to MPS sites. In Fig. 8, we display the normalized block entropy $\tilde{S}(l) \equiv S(l)/\max[S(l)]$ and the similarly rescaled single-site entropy $\tilde{s}_i \equiv s_i/\max[S(l)]$ of the ground state of the half-filled 6×6 Hubbard model in momentum space for small values of U . As can be seen, the rescaled profiles of both quantities fall onto a single curve to a good approximation, although the actual values of both the block and the site entropies change significantly.

To understand the scaling behavior, we consider the subadditivity of the entropy [64], i.e., the change in the block entropy in each full step of the DMRG, in which an enlarged block with $l+1$ sites is formed from a block with l sites and the $(l+1)^{\text{th}}$ site [65]. This entropy reduction is due to the correlations between the block and the site and is given by the mutual information

$$I(l) = S(l) + s_{l+1} - S(l+1). \quad (5)$$

In the DMRG, the set of block states is chosen by taking the eigenstates of the reduced density matrix with the largest eigenvalues. It can be shown that this operation can be implemented as a LOCC (local operation and classical communication) so that it cannot lead to an increase in entanglement. With no truncation, it holds that $I_{\text{tot}} \equiv \sum_l I(l)$ for a full sweep is equal to the sum of the single-site entropies, $\sum_i s_i$. Thus, I_{tot} quantifies the total quantum information encoded in the wave function. Therefore, the scaling of the site entropy as a function of U and system size also determines the scaling of the block entropy. We will come back to the detailed scaling for weak U once we have investigated the system-size and U dependence of the maximum of the block entropy,

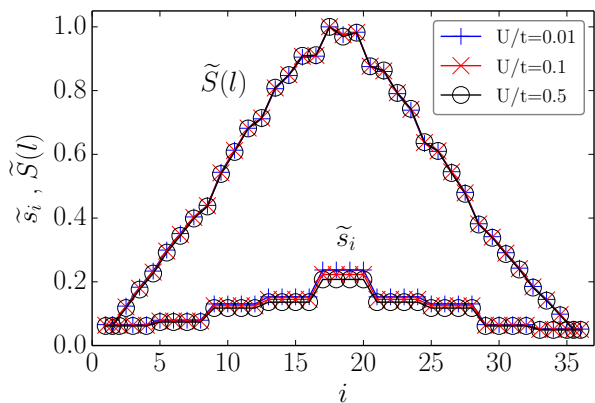


FIG. 8. (Color online) Normalized block entropy $\tilde{S}(l)$ (upper curves) and single-site entropy \tilde{s}_i (lower curves) of the ground state of the 6×6 Hubbard model in momentum space for small values of U at half-filling.

$\max[S(l)]$.

Next, we examine the large- U behavior of the single-site and block entropies, depicted in Fig. 9. In this case, not only the amplitude but also the shape of the profiles changes; thus, we do not rescale the data. As can be seen, above a critical value of U , some of the site entropies reach the maximum value of $\ln 4$, and the site entropy profile starts to broaden. (In the $U \rightarrow \infty$ limit, all sites will have $s_i = \ln 4$.) Since the growth of the block entropy per site is bounded by the single-site entropy due to Eq. (5), the block entropy profile and its maximum must also saturate. Furthermore, in the half-filled case for these larger- U values, zig-zag peaks appear superimposed upon the profile. These peaks correspond to those bipartite partitions of the system that cut the system between two sites that fulfill the nesting condition (which are the strongest correlated sites, as reflected in I_{ij}). Therefore, the peaks are related to the zig-zag pattern seen in the first minor diagonals of I_{ij} in Fig. 4(a).

We now turn to the effect of doping. In Fig. 10, we display a comparison of block entropy profiles for the half-filled and doped system for weak and intermediate coupling strength. At $U = 1$, the profiles are similar, with no additional structures present. At $U = 4$, it is evident that the additional oscillating structures are only present at half-filling. This is due to the fact that the perfect nesting of the Fermi surface is destroyed in the doped system, so that the corresponding bonds are less entangled, as discussed before, and no additional peaks develop. Note that for each parameter set, the block entropy is calculated for the corresponding optimal ordering and thus the MPS site indices i do not correspond to the same \mathbf{k} points.

We now analyze the entanglement scaling as a function of system size N , starting with the one-dimensional model and then moving to the two-dimensional case. In both cases, the data points in the figures refer to the maximum of the block entropy taken from the last half sweep

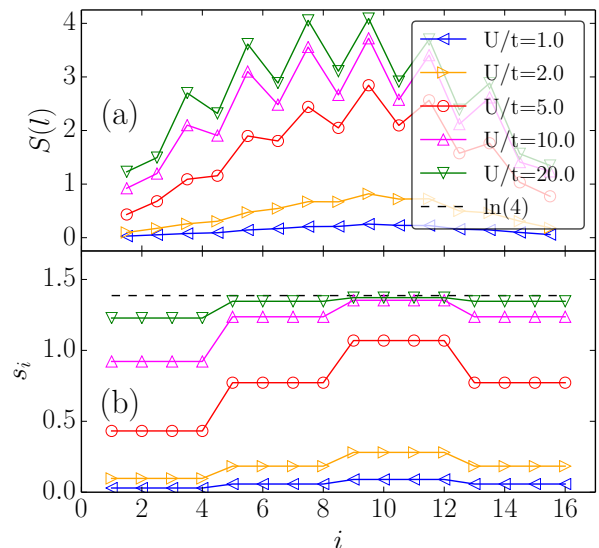


FIG. 9. (Color online) Block entropy $S(l)$ (a) and single-site entropy s_i (b) of the ground state of the 4×4 Hubbard model in momentum space for large values of U at half-filling.

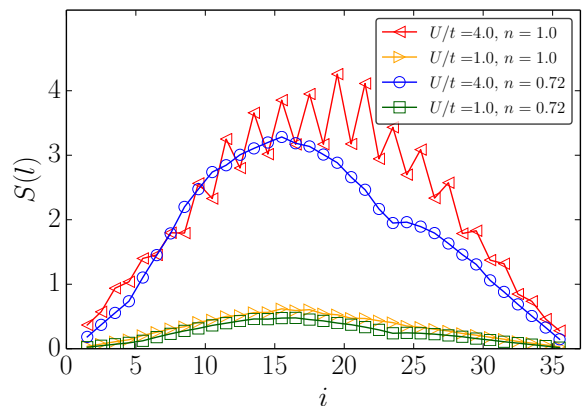


FIG. 10. (Color online) Block entropy profiles $S(l)$ of the 6×6 Hubbard model in momentum space for weak coupling $U/t = 1.0$ and intermediate coupling $U/t = 4.0$ for the half-filled $n = 1.0$ and doped $n = 0.722$ case. Every profile is calculated using the optimal ordering for the particular set of parameters U, n .

of each calculation, while the error bars are given by the difference between these values and the zero-truncation extrapolated values. (The extrapolated values are obtained by repeatedly measuring the maximum of the block entropy during the sweeping process while simultaneously increasing the number of block states kept and thus lowering the truncation error.) This procedure for error estimation generally tends to overestimate the actual error. Figure 11 depicts the maximum of the block entropy, $\max[S(l)]$, for the half-filled, $n = 1.0$, and for the doped, $n = 0.75$, one-dimensional Hubbard model as a function of the number of sites N for various values of U . The dashed lines, which are linear fits to the data,

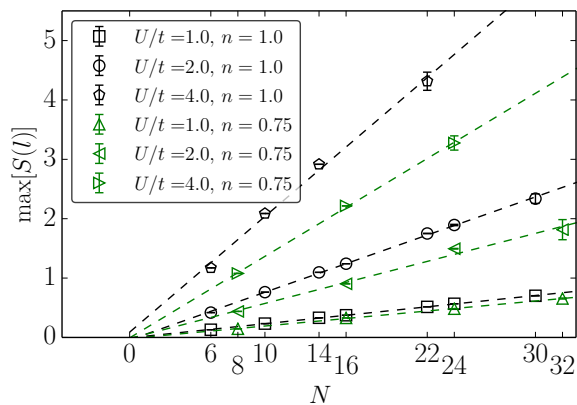


FIG. 11. (Color online) Maximum of the block entropy, $\max[S(l)]$, as a function of the system volume N for different values of U for the one-dimensional Hubbard model in momentum space at half-filling and at three-eighths filling, $n = 0.75$. The dashed lines are linear fits to the data.

show that the maximum of the block entropy scales with the volume of the system. This scaling with volume for a wide range of U values clearly shows that the entropy area law does not hold for this case. Interestingly, in momentum space, the block entropy is appreciably smaller for the doped system than for the half-filled system of the same size and interaction strength. Consequently, the doped system is easier to treat computationally than the half-filled system, in contrast to real space, in which the doped case is generally harder to treat numerically.

For the two-dimensional system, Fig. 12 depicts the scaling of the maximum of the block entropy with system size for different values of U for the half-filled, $n = 1.0$, and for the doped, $n \approx 0.75$, systems. The dashed lines are linear fits to the data for the half-filled system, indicating almost perfect scaling with the system size. For the doped case, the block entropy for a particular value of U is again noticeably smaller than for the half-filled system. As we have seen earlier in the entropy profiles, this effect becomes stronger for larger values of U . Note that for the 4×4 system, the nesting of the Fermi surface is not destroyed in the doped case; therefore, the block entropies for the half-filled and doped cases do not differ much.

Regarding the question of the origin of the volume scaling of the maximum block entropy, we argue as follows: Within the momentum-space picture, what is important is how strongly a given region in momentum space is correlated with other regions, especially regions that correspond to DMRG blocks at optimal site ordering. As the system size is increased, the density of the \mathbf{k} points in each region of momentum space increases linearly with system size, ultimately leading to a linear increase in the total correlation. Furthermore, the correlation patterns in momentum space depicted in Figs. 1(b), 3(b), 4(b), and 5(b) show that strong correlations occur between regions close to each other as well as widely separated from each other. In particular, correlation bonds of compar-

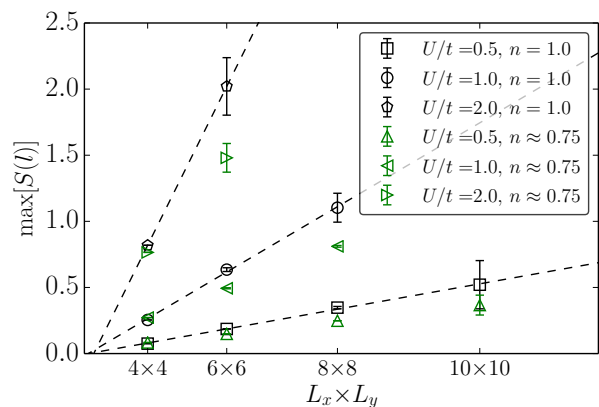


FIG. 12. (Color online) Maximum of the block entropy, $\max[S(l)]$, as a function of the system volume $N = L_x L_y$ for different values of U for the two dimensional Hubbard model in momentum space at half-filling and near $n = 0.75$ filling ($n = 0.75$ for 4×4 , $n = 0.722$ for 6×6 , $n = 0.75$ for 8×8 , $n = 0.74$ for 10×10). The dashed lines are linear fits to the data at half-filling.

able strength form loops, which cannot be disentangled globally when the momentum-space lattice is mapped onto the sites of the MPS. Thus, even for optimal site ordering, regions of sites separated by a macroscopic number of sites in the MPS lattice, i.e., a separation of up to an appreciable fraction of the system size, will still be correlated with one another. The growth of the total correlation with the site density, in combination with the fact that the corrections are long range in the MPS, finally leads to a linear scaling of the block entropy $S(l)$ with system size for all decompositions and to volume-law scaling of the maximum block entropy. The linear growth of the total correlation with subsystem size is also reflected in the approximately triangular-shaped block entropy profiles in Figs. 8 and 10. Note that reordering the system in an optimal way is still crucial in order to obtain good convergence, even though it cannot avoid the volume scaling of the entropy in the momentum-space Hubbard model.

Having established the volume scaling of the block entropy, we finally investigate the U dependence of the volume-scaled maximum block entropy, taking the half-filled case. We divide out the volume scaling in $\max[S(l)]$ by taking $\max[S(l)]/N$ so that we can compare the behavior for different system sizes. We start with the one-dimensional case, depicted in Fig. 13. For $U \rightarrow 0$, the block entropy must vanish because the noninteracting ground state is a product state in momentum space. For weak coupling, the maximum block entropy scales with U^2 , as can be seen in the inset, where a fit to U^2 is shown. For large U , the maximum of the block entropy saturates for a given system size, but the upper limit seems to be significantly smaller than its theoretical limit of $\ln 2$. Furthermore, while the curves for different system sizes fall on top of each other (as expected given a volume law for the system size scaling) for small U , for large U the limiting value decreases somewhat with system size, in-

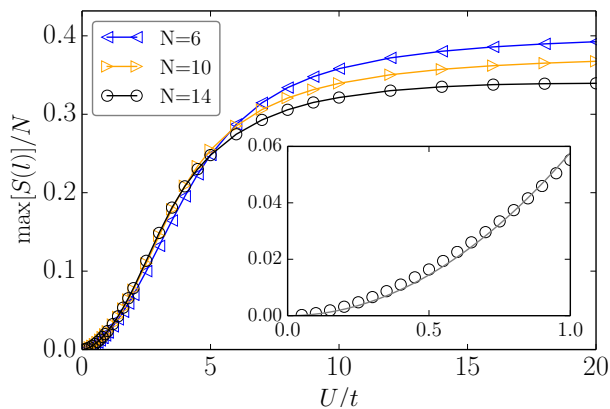


FIG. 13. (Color online) Maximum of the block entropy $S(l)$ per site as a function of U calculated exactly for the $N = 6, 10, 14$ site Hubbard model in momentum space at half-filling. The inset shows a quadratic fit (gray line) for $0 \leq U \leq 1$ and $N = 14$.

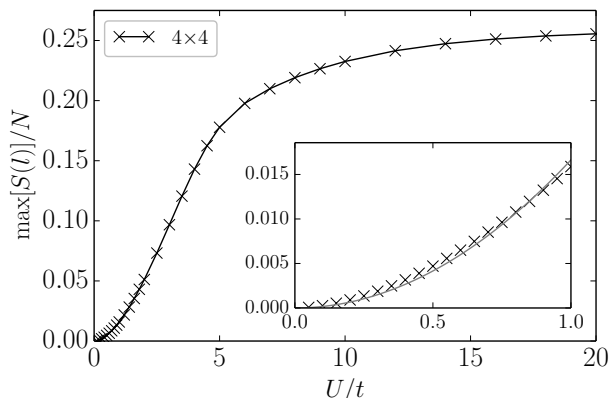


FIG. 14. Maximum of the block entropy $S(l)$ per site as a function of U calculated exactly for the 4×4 Hubbard model in momentum space at half-filling. The inset shows a quadratic fit (gray line) for $0 \leq U \leq 1$.

dicating a sub-linear scaling. However, only relatively small system sizes are accessible in the large- U limit, so that a definitive analysis of this effect cannot be carried out.

For the two-dimensional case, an analysis for the complete range of U values can only be carried out for the exactly treatable 4×4 system. For this system, the behavior of the maximum block entropy as a function of U , shown in Fig. 14, is similar to that in one dimension, with quadratic scaling in U in the weak-coupling regime and saturation of the maximum of the block entropy in the strong-coupling limit. We have previously shown that the block entropy $S(l)$ and the single-site entropy s_i show the same scaling behavior as a function of U for all l or i , respectively. Therefore, $S(l)$ and s_i also scale quadratically with U at weak coupling. Note that the saturation value for large U is actually significantly smaller in the two-dimensional case than in the one-dimensional case.

IV. DISCUSSION AND CONCLUSION

In this paper, we have applied an efficient, optimized version of the momentum-space DMRG to the Hubbard model in one and two dimensions. The effectiveness of our method has allowed us to carry out an extensive study of the entanglement structure for both the one-dimensional and two-dimensional models at half-filling and at moderate doping. In particular, we have examined a number of quantum-information-based measures in order to understand the entanglement and pair-wise correlation of sites in the single-particle momentum basis.

By analyzing the correlations between individual sites in terms of the two-site mutual information, we have been able to determine what type of excitations of the noninteracting system are most important within the interacting ground state. For the one-dimensional half-filled system, we have found that the strongest correlations are between pairs of sites that are close to the Fermi points but are separated by π in momentum space. Excitations over these sites, due to their relative positioning in momentum space, are energetically favorable and have a momentum transfer of 2π , which is necessary for umklapp scattering processes. In the doped case, the pairs of sites close to the now shifted Fermi points are no longer separated by π , and therefore umklapp scattering and the corresponding excitations are forbidden by momentum conservation. With fewer favorable excitations allowed in the ground-state space, the correlations drop significantly, leading to lower block entanglement for the corresponding bipartite decompositions of the system. For the two-dimensional system, the perfect nesting of the Fermi surface in the half-filled case is responsible for an analogous effect. Pairs of sites near the Fermi surface that are separated in the \mathbf{k} plane by (π, π) thus allow for a larger number of energetically low-lying excitations. When the system is doped, the deformation of the Fermi surface destroys the nesting and truncates the number of energetically favorable excitations allowed in the ground-state space. Apart from these observations, we have used the results directly to obtain an optimal ordering of momentum sites within the MPS chain for each situation in order to significantly improve the DMRG convergence.

In a second step, we have investigated the behavior of the von Neumann entropies, in particular, the single-site entropy and the subsystem entropy of the DMRG blocks. The most important indicator for the computational costs and convergence of the DMRG is the scaling of the maximum of the block entropy, which we have analyzed as a function of the system volume and coupling strength. For the half-filled and doped systems we have found that the maximum block entropy scales proportionally to the number of sites. We understand this from the two-site mutual information measurements, which indicate that there is an increase in total correlation between regions in momentum space proportional to the density of momentum points and that the correlations in

our system are long range in the MPS structure in spite of the optimization of the site ordering. The combination of these two effects leads to volume-law scaling of the block entropy.

Once the volume dependence is factored out, we obtain almost universal curves for the maximum of the block entropy per site for both the one- and two-dimensional Hubbard models, at least at half-filling. These curves must go to zero at zero interaction and increase with the square of the interaction strength for weak coupling, retaining a perfect volume scaling. The presence of volume scaling of the entropy at arbitrary weak interaction is a distinct indication of the fundamental limitations of perturbative approaches for the Hubbard model in one and two dimensions. For strong coupling, the maximum entropy per site saturates, with a boundary value lying clearly below its theoretical limit and with a volume scaling that seems to be slightly sublinear, at least in the one-dimensional, half-filled case. We find this result somewhat surprising and slightly less unfavorable than naively expected, even though, admittedly, the high value of the maximum entropy per site and the approximate volume law preclude any well-controlled MPS-based approaches.

Despite these limitations, the momentum-space DMRG also has some interesting favorable properties. While the convergence of the real-space DMRG becomes worse for doped systems, we have found that, in momentum space, the block entanglement decreases and the convergence improves upon doping. In addition, our highly optimized and parallelized code has enabled us to keep a comparably large number of block states at reasonable

computational cost, a number of states that is typically significantly larger than a comparably optimized real-space DMRG code for similar system size and parameters. Since the coefficient of the volume scaling can be made arbitrarily small at weak interaction, the k-DMRG could nevertheless yield variationally competitive results, at least relative to the real-space DMRG, for particular moderate system sizes at sufficiently weak interaction.

One possibility to overcome the main problems of momentum-space DMRG while keeping some of its advantages is to use a hybrid real- and momentum-space representation, i.e., take a momentum basis in the transverse direction and a real-space basis in the other direction. In this way, the translational invariance and good momentum quantum numbers are preserved in the transverse direction, but the volume-law entanglement due to long-range interactions in the longitudinal direction can be avoided.

ACKNOWLEDGMENTS

We thank S. R. White, D. J. Scalapino, G. Barcza, S. R. Manmana, P. R. Corboz, and Sz. Szalay for useful discussions. This work was supported in part by the Deutsche Forschungsgemeinschaft (DFG) through Grant No. NO 314/5-1 in Research Unit FOR 1807 and the Hungarian Research Fund (OTKA) through Grants No. K100908 and No. NN110360.

-
- [1] G. Vidal, Phys. Rev. Lett. **91**, 147902 (2003).
 - [2] J. P. F. LeBlanc *et. al.* (The Simons Collaboration on the Many-Electron Problem), arXiv:1505.02290 (2015).
 - [3] L. Amico, R. Fazio, A. Osterloh, and V. Vedral, Rev. Mod. Phys. **80**, 517 (2008).
 - [4] S. Östlund and S. Rommer, Phys. Rev. Lett. **75**, 3537 (1995).
 - [5] F. Verstraete and J. I. Cirac, arXiv:cond-mat/0407066v1 (2004).
 - [6] S. R. White, Phys. Rev. Lett. **69**, 2863 (1992).
 - [7] T. Nishino, Y. Hieida, K. Okunishi, N. Maeshima, Y. Akutsu, and A. Gendiar, Prog. Theor. Phys. **105**, No. 3, 409 (2001).
 - [8] G. Vidal, Phys. Rev. Lett., **101**, 110501 (2008).
 - [9] F. Verstraete, J. I. Cirac, and V. Murg, Adv. Phys. **57**, 143 (2008).
 - [10] Y.-Y. Shi, L.-M. Duan, and G. Vidal, Phys. Rev. A **74**, 022320 (2006); L. Tagliacozzo, G. Evenbly, and G. Vidal, Phys. Rev. B **80**, 235127 (2009).
 - [11] S. R. White, D. J. Scalapino, R. L. Sugar, E. Y. Loh, J. E. Gubernatis, and R. T. Scalettar, Phys. Rev. B **40**, 506 (1989).
 - [12] C.-C. Chang and S. Zhang, Phys. Rev. B **78**, 165101 (2008); Phys. Rev. Lett. **104**, 116402 (2010).
 - [13] H. Shi and S. Zhang, Phys. Rev. B **88**, 125132 (2013).
 - [14] F. Becca, M. Capone, and S. Sorella, Phys. Rev. B **62**, 12700 (2000).
 - [15] L. F. Tocchio, F. Becca, and C. Gros, Phys. Rev. B **83**, 195138 (2011).
 - [16] G. Knizia and G. K.-L. Chan, Phys. Rev. Lett. **109**, 186404 (2012).
 - [17] G. Knizia and G. K.-L. Chan, J. Chem. Theory Comput. **9**, pp. 1428–1432 (2013).
 - [18] E. Y. Loh Jr., J. E. Gubernatis, R. T. Scalettar, S. R. White, D. J. Scalapino, and R. L. Sugar, Phys. Rev. B **41**, 9301 (1990).
 - [19] M. Troyer and U.-J. Wiese Phys. Rev. Lett. **94**, 170201 (2005).
 - [20] R. Orús, Ann. Phys. (Amsterdam) **349**, 117 (2014).
 - [21] P. Corboz and F. Mila, Phys. Rev. Lett. **112**, 147203 (2014).
 - [22] R.M. Noack, S.R. White, and D.J. Scalapino, in *Computer Simulations in Condensed Matter Physics VII*, Eds. D.P. Landau, K.K. Mon, and H.B. Schüttler (Springer Verlag, Heidelberg, Berlin, 1994), p. 85-98.
 - [23] S. R. White, Nature Physics **8**, 863864 (2012).
 - [24] S. Depenbrock, I. P. McCulloch, and U. Schollwöck, Phys. Rev. Lett. **109**, 067201 (2012).
 - [25] G. Evenbly and G. Vidal, Phys. Rev. Lett. **104**, 187203 (2010).

- [26] N. Schuch, D. Poilblanc, J. I. Cirac, D. Perez-Garcia, Phys. Rev. B **86**, 115108 (2012).
- [27] Ö. Legeza and J. Sólyom, Phys. Rev. B **68**, 195116 (2003).
- [28] Sz. Szalay, M. Pfeiffer, V. Murg, G. Barcza, F. Verstraete, R. Schneider, and Ö. Legeza. Int. J. Quant. Chem. bf 115, pp. 1342–1391 (2015).
- [29] E. Fertitta, B. Paulus, G. Barcza, and Ö. Legeza, Phys. Rev. B **90**, 245129 (2014).
- [30] C. Krumnow, Ö. Legeza, and J. Eisert, arXiv:1504.00042 (2015).
- [31] J. Eisert, M. Cramer, and M.B. Plenio, Rev. Mod. Phys. **82**, 277 (2010).
- [32] Ö. Legeza, F. Gebhard, and J. Rissler, Phys. Rev. B **74**, 195112 (2006).
- [33] J. Sólyom, *Fundamentals of the Physics of Solids* (Springer, Heidelberg, 2010), Vol. 3.
- [34] T. Xiang, Phys. Rev. B **53**, R10445(R) (1996).
- [35] S. Nishimoto, E. Jeckelmann, F. Gebhard, and R. M. Noack, Phys. Rev. B **65**, 165114 (2002).
- [36] U. Schollwöck, Rev. Mod. Phys. **77**, 259–315 (2005).
- [37] R. M. Noack and S. R. Manmana, in *Diagonalization- and Numerical Renormalization-Group-Based Methods for Interacting Quantum Systems*, edited by A. Avella and F. Mancini (AIP, 2005), vol. 789, pp. 93–163.
- [38] K. Hallberg, Adv. in Phys. **55**, pp. 477–526 (2006).
- [39] U. Schollwöck, Ann. Phys. (NY) **326**, 96 (2011).
- [40] M. A. Nielsen and I. L. Chuang, *Quantum Computation and Quantum Information* (Cambridge University Press, New York, 2000).
- [41] J. Preskill, *Lecture notes on Quantum Computation*, <http://www.theory.caltech.edu/people/preskill/ph229>.
- [42] M. M. Wilde, *Quantum Information Theory* (Cambridge University Press, New York, 2013).
- [43] R. Horodecki, P. Horodecki, M. Horodecki, and K. Horodecki, Rev. Mod. Phys. **81**, 865 (2009).
- [44] Sz. Szalay, arXiv:1302.4654 (2013).
- [45] G. Vidal, J. I. Latorre, E. Rico, and A. Kitaev, Phys. Rev. Lett. **90**, 227902 (2003).
- [46] Ö. Legeza, J. Röder, and B. A. Hess, Phys. Rev. B **67**, 125114 (2003).
- [47] J. Rissler, R.M.Noack, and S.R. White, Chem. Phys. **323**, 519–531 (2006).
- [48] V. Murg, F. Verstraete, Ö. Legeza, and R. M. Noack, Phys. Rev. B **82**, 205105 (2010).
- [49] D. Larsson and H. Johannesson, Phys. Rev. Lett. **95**, 196406 (2005).
- [50] K. Modi, T. Paterek, W. Son, V. Vedral, and M. Williamson, Phys. Rev. Lett. **104**, 080501 (2010).
- [51] M. M. Wolf, F. Verstraete, M. B. Hastings, and J. I. Cirac, Phys. Rev. Lett. **100**, 070502 (2008).
- [52] R. Lundgren, J. Blair, M. Greiter, A. Läuchli, G. A. Fiete, and R. Thomale, Phys. Rev. Lett. **113**, 256404 (2014).
- [53] G. Barcza, Ö. Legeza, K. H. Marti, and M. Reiher, Phys. Rev. A **83**, 012508 (2011).
- [54] V. Murg, F. Verstraete, R. Schneider, P. R. Nagy, and Ö. Legeza, J. Chem. Theory Comput. **11**, pp. 1027–1036 (2015).
- [55] G. Gori, S. Paganelli, A. Sharma, P. Sodano, and A. Trombettoni, Phys. Rev. B **91**, 245138 (2015).
- [56] K. Boguslawski, P. Tecmer, Ö. Legeza, and M. Reiher, J. Phys. Chem. Lett. **3**, 3129–3135 (2012).
- [57] K. Boguslawski, P. Tecmer, G. Barcza, Ö. Legeza, and M. Reiher, J. Chem. Theory Comput. **9**, 2959–2973 (2013).
- [58] Y. Kurashige, G. K.-L. Chan, and T. Yanai, Nature Chemistry **5**, 660–666 (2013).
- [59] G. Barcza, J. Sólyom, R. M. Noack, and Ö. Legeza, arXiv:1406.6643 (2014).
- [60] S. R. White and R. Martin, J. Chem. Phys. **110**, 4127 (1999).
- [61] S. R. White, Phys. Rev. B **72**, 180403(R) (2005).
- [62] See <http://itensor.org>.
- [63] F. H. L. Essler, H. Frahm, F. Göhmann, A. Klümper, and V. E. Koropin, *The One-Dimensional Hubbard Model* (Cambridge University Press, Cambridge, 2005).
- [64] T. Sagawa, *Second Law-Like Inequalities with Quantum Relative Entropy: An Introduction in Lectures on Quantum Computing, Thermodynamics and Statistical Physics*, edited by M. Nakahara and S. Tanaka (World Scientific Publishing Company, Singapore, 2012), Vol. 8.
- [65] Ö. Legeza and J. Sólyom, Phys. Rev. B **70**, 205118 (2004).